

Non-Iterative Localization and Fast Mapping

Chen Wang, *Student Member, IEEE*, Lihua Xie, *Fellow, IEEE*, and Junsong Yuan, *Senior Member, IEEE*

Abstract—This paper presents a non-iterative method for dense mapping using inertial sensor and depth camera. To obtain data correspondence, traditional methods resort to iterative algorithms which are computationally expensive. This paper proposes a novel non-iterative framework with a computationally efficient closed-form solution to the front-end of the dense mapping system. First, 3-D point clouds with 6 degrees of freedom are decoupled into independent subspaces, in which point clouds can be matched respectively. Second, without any prior knowledge, the matching process is carried out by single key-frame training in frequency domain, which reduces computational requirements dramatically and provides a closed-form solution. Third, 3-D maps are presented and fused in the subspaces directly to further reduce the complexity. In this manner, the complexity of our method is only $\mathcal{O}(n \log n)$ where n is the number of matched points. Extensive tests show that, compared with the state-of-the-arts, the proposed method is able to run at a much faster speed and yet still with comparable accuracy.

Index Terms—Non-Iterative Solution, Localization and Mapping, Inertial Fusion, 3-D Camera

I. INTRODUCTION

SELF-LOCALIZATION-MAPPING is one of the most basic capabilities of autonomous robots, and has received increasing attention in tandem with the development of hardware, such as smarter sensors and faster processors [1]. However, visual dense mapping algorithms are still difficult to be applied directly to micro-robot systems, especially micro unmanned aerial vehicles (MUAV). This is because micro-robot systems can only provide limited computational resources, such as ultra low power embedded processors, due to payload and power limitations. Moreover, dense maps, which are crucial for higher level applications, such as collision-free motion planning, object detection and scene understanding, require more computational resources to produce [2]. This paper aims to develop a lightweight dense mapping system that can be carried by micro-robot systems, and achieves faster computational speed with sufficient accuracy. Leveraging on depth camera and inertial sensor, this paper finds a non-iterative solution for visual data association.

In the simultaneous localization and mapping (SLAM) problem, data association, which is to relate the sensors' measurements with the landmarks inside the maps [3], is one of the most important and time consuming parts. From the following analysis, nearly all the existing visual SLAM or dense mapping algorithms resort to iterative solutions to find data association, which is the main source of computational burden. First, iterative closest point (ICP) is one of the most widely used algorithms where point clouds need to be matched

[4]. The problem of ICP and its variants lies in the high complexity, so that many modern algorithms such as [5]–[9] need powerful GPU to process the large number of data. Second, feature-based [2], [10]–[13] and direct methods [12], [14]–[18] have been proposed for monocular, stereo cameras, and depth cameras [14], [19]. However, they need iterative methods, e.g. Gauss-Newton, to match the images, so that the camera motion can be estimated. Third, the tightly-coupled inertial fusion SLAM algorithms using monocular camera [20], stereo camera [21], and depth camera [22] also need iterative numerical solutions to solve the non-linear optimization problem. Fourth, to remove outliers, iterative methods like RANSAC [23] are also widely used [13], [19]. Last, the deep learning based odometry or SLAM methods [24]–[28] also need iterative solutions to adjust the weights of each neuron in the networks.

The above discussion shows that the iterative solutions, including but not limited to the mentioned above, are the main source of computational burden of data association. To reduce the requirements, we argue that the traditional visual or visual-inertial data association problem should be reformulated, since a suitable closed-form solution may be able to reduce the computational requirements dramatically. Moreover, a closed-form solution doesn't require well-designed initialization to prevent local minimum. However, the objective functions of traditional methods, e.g., tightly-coupled inertial fusion, feature-based and direct methods, are highly non-linear and difficult to find feasible closed-form solutions. To this end, a new objective function with closed-form solution is proposed for dense RGB-D-inertial mapping. In short, the rotational movements are decoupled from translational movements by leveraging on the attitude and heading reference system (AHRS), so that the translational motion model can be predicted based on single key-frame training. Then the movements are obtained by re-coupling the estimation in rotational and translational spaces.

A preliminary version of this work named as non-iterative SLAM (NI-SLAM) is presented in [29]. It demonstrates that, for the first time, a non-iterative solution to RGB-D-inertial data association is able to reduce the computational requirements dramatically. It enables fast dense mapping on micro robots with an ultra-low power processor. This paper adds to the initial version in a significant way. First, the axnometric reprojection process is extended to dynamic resolution, resulting in a more accurate estimation and detailed map. Second, the non-iterative solution based on kernelized correlaion filter (KCF) [30] is re-derived in a much simpler way using our recently proposed kernel cross-correlator (KCC) [31]. The KCF, which is limited to non-weighted kernel functions and circulant training data, is a special case of KCC which breaks the limitations and extends the traditional cross-correlation to kernel case. Third, the superiority of the proposed method on efficiency is demonstrated by comparing

Chen Wang, Lihua Xie, and Junsong Yuan are with the School of Electrical and Electronic Engineering, Nanyang Technological University, 50 Nanyang Avenue, Singapore 639798. e-mail: wang.chen@zoho.com; elhxie@ntu.edu.sg; jsyuan@ntu.edu.sg

with several state-of-the-art algorithms. The experiments are extended for stereo cameras to demonstrate the flexibility. Last, a flexible framework is proposed for RGB-D-inertial dense mapping system.

II. RELATED WORK

This paper focuses on data association, dense mapping, and inertial fusion, while loop closure detection will not be presented. The works on monocular/stereo camera will be reviewed, since many methods can be used for depth camera.

A. Data Association and Map Fusion

Many dense mapping systems resort to ICP and its variants to align point clouds with respect to photometric or geometric constraints. KinectFusion [5] is one of the most famous methods. It permits dense volumetric reconstruction of complex room-sized scenes based on a volumetric truncated signed distance function (TSDF). The incremental pose transformation is obtained by tracking the live depth frame relative to the global model using a coarse-to-fine ICP algorithm with geometric constraints. Following this work, Kintinuous [6] enables dense mesh-based mapping for extended scale environments and implements a triangular mesh generation module for the map representation. ElasticFusion [7] combines dense geometric constraints with photometric constraints to achieve robust pose estimation in more challenging scenes. Furthermore, [32] brings Kintinuous and ElasticFusion together, and adds a method for improving camera-frustum overlap for a greater reconstruction range. The pose estimation is obtained by a dense every-frame volumetric fusion front-end, and the dense surface is corrected by non-rigid map deformation back-end. DynamicFusion [9] generalizes the TSDF to nonrigid case, so that dynamic scenes can be reconstructed and a volumetric 6D motion field can be estimated. BundleFusion [33] applies a local-to-global pose alignment framework and a paralleled sparse-to-dense optimization for sparse feature correspondence and dense geometric and photometric matching. Since the above methods heavily rely on ICP and require powerful GPU to process large number of data, they are not applicable to systems with low computational power.

To decrease the computational requirements, dense visual odometry (DVO) [15] proposes a faster, robust method based on a t-distribution-based photometric error model that can be obtained by the iteratively re-weighted least square (IRLS) algorithm. An improved version of DVO [14] extends the t-distribution model to depth error and propose a entropy-based similarity measurement for key-frame selection and loop closure detection. The proposed t-distribution model can be reduced to the standard least square (LS) minimization problem when error residual is assumed to be normally distributed.

Feature-based method is the most widely-used LS minimization algorithm in visual SLAM to minimize reprojection error. Its basic idea is that the incremental pose transformation can be estimated by matched features. During the feature-detection step, salient key features that are likely to be matched well with other images are selected. Basically, there are two main approaches to find the corresponding features [34]. One

is to extract features by local search techniques [12] and match them between the latest image and key-frame [13]. It is suitable for images taken from nearby viewpoints. The other one is to extract features independently and match them in sequences of images based on similarity descriptors [35], which is suitable for large motion between two viewpoints.

Based on feature tracking, PTAM [11] first proposes to track the camera poses parallel to the mapping thread in a bundle adjustment framework. This enables real-time landmarks tracking and pose estimation at the frame-rate. ORB-SLAM [13] carries forward this work by designing a robust system that uses the same features for all SLAM tasks: tracking, mapping, relocalization, and loop closing. This leads to a reliable and complete solution, but it still only produces sparse maps. One of the earliest dense feature-based SLAM systems is RGB-D mapping [2] where Generalized-ICP and RANSAC are combined to optimize the pose graph. RGB-D-SLAM [19] highly exploits feature correspondences by sparse bundle adjustment (BA) and has become one of the most successful feature-based methods for a depth camera.

In contrast with feature-based methods, direct methods match raw image pixels directly. Since there is no descriptor, only local search techniques can be used to find the corresponding pixels; hence this is not suitable for large motion between two viewpoints. DTAM [18] develops a real-time camera tracking and reconstruction system where pose estimation is from the minimization of photometric error on every pixel. Within a depth probabilistic framework, SVO [12] achieves semi-dense maps with accurate motion estimation by minimizing photometric error outside of non-negligible gradients regions. LSD-SLAM [17] enables to build consistent large-scale maps by aligning image directly based on photoconsistency and estimating a filtering-based semi-dense depth map. By incorporating disparity sources from fixed-baseline stereo, Stereo-LSD [36] avoids the scale-drift problem and built a consistent map for large scale environments using stereo cameras. DSO [37] proposes a direct sparse odometry system that minimizes the photometric error on sampled pixels with large intensity gradients. Although these methods reduce the computational requirements a lot, they still need iterative solutions to fit a pose transformation model, so that their time complexity is still too high to produce dense maps on low power embedded processors.

The deep learning based visual odometry or SLAM methods have also been studied. In [24], the authors explore the use of convolutional neural networks (CNN) to learn the visual features for ego-motion estimation. DeepVO [25] proposes a CNN-based architecture for estimating the objects pose under known environment. CNN-SLAM [26] combines the direct methods with CNN-predicted depth maps to overcome the absolute scale problem of monocular SLAM. [28] proposes to train two CNNs, one of which operates on single images and extracts salient 2-D points, while another one operates on pairs of the points and estimates the homography. The recent trend towards deep learning mitigates a new wave of research, but the real-time performance may still be low. This challenge opens space for learning techniques that aim to achieve higher accuracy and yield faster training. This paper enables the real-

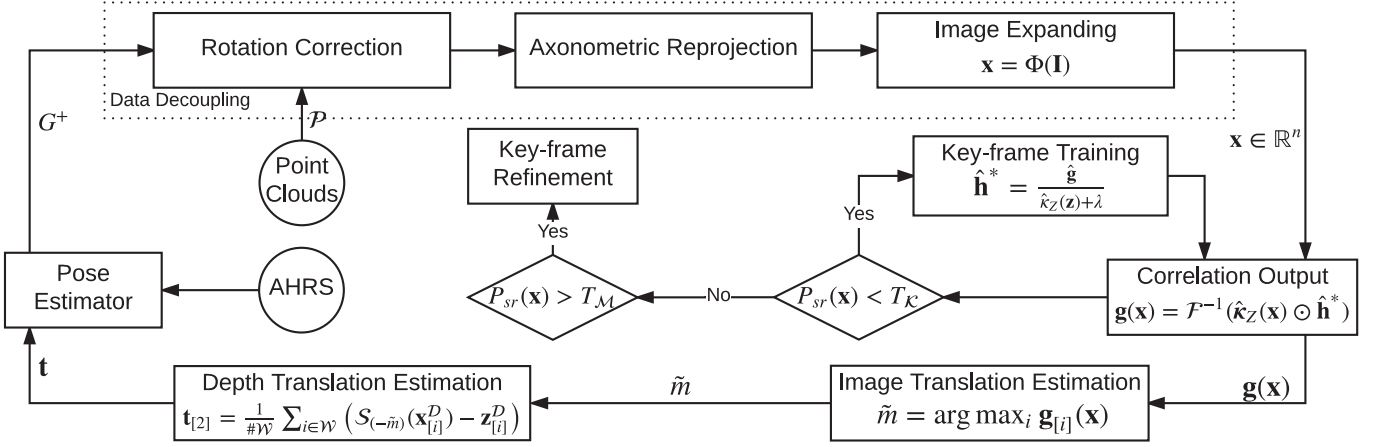


Fig. 1. The proposed non-iterative framework for localization and dense mapping system. The 3-D movements are estimated in decoupled subspaces separately. Because of a set of algorithms to reduce computation, the complexity of whole process is reduced to $\mathcal{O}(n \log(n))$ where n is the number of points.

time trainable methods on low power processors.

B. Inertial Fusion

Inertial sensors provide additional constraints for the camera pose estimation and can help improve the performance of visual odometry or SLAM systems. The most computationally efficient inertial fusion approach is the loosely coupled methods, that process inertial and visual measurement separately. [38] presents an extended Kalman filter (EKF)-based constant complexity framework that treats the visual odometry system as a black box. This leads to a reduction on computational cost and is suitable for power limited robotic systems. MSF-EKF [39] presents a generic and modular multi-sensor fusion framework to deal with delayed absolute or relative measurements. Alternatively, attitude estimation can be extracted and then fused into visual estimation algorithms. [40] shows that angular precision of long term VO can be improved dramatically by such loosely coupled fusion.

In contrast to loosely coupled methods, tightly-coupled methods estimate the states jointly. MSCKF [41] derives a measurement model that is able to express the geometric constraints from static image features. It jointly estimates the IMU states and a sliding window of camera poses by an EKF estimator, resulting in a linear complexity in the number of features. MSCKF 2.0 [42] improved MSCKF and corrected the inconsistent linearized system model that has incorrect observability properties. OKVIS [21] constructs a joint probabilistic cost function that combines visual reprojection errors and inertial measurements to observe landmarks using monocular or stereo cameras. [20] proposes a joint non-linear optimization system using direct method, resulting in a semi-dense map. [43] develops a preintegration theory for IMU on the manifold structure of rotation group that is able to summarize the large number of inertial measurements between two key-frames as a single geometric constraint. [44] combines inertial tracking in a dense SLAM framework, that is able to reconstruct large scale out-door scenes. [22] proposes the first tightly-coupled dense RGB-D-inertial SLAM system, which needs powerful GPU to process map deformations.

The tightly-coupled methods have an additional complexity due to the involvement of large number of visual measurements. Based on recurrent and convolutional networks, VINet [27] presents an on-manifold sequence-to-sequence learning approach to motion estimation for inertial fusion.

III. SYSTEM ARCHITECTURE

Iterative methods in this paper are defined as those odometry or SLAM algorithms that need iterative solutions to find data association. This section summaries the traditional iterative solutions and proposes a non-iterative framework.

A. Iterative Framework

The SLAM algorithms for depth cameras, such as [5]–[9], [32], [33] that heavily depend on variants of ICP are the most representative examples of iterative methods. Let $\{\mathcal{M}, \mathcal{S}\}$ be two finite size points sets with both position and color information, the objective of ICP is to find a transformation $\mathcal{T}(\cdot)$ to be applied to the points \mathcal{M} , such that the difference $D(\cdot)$ between $\mathcal{T}(\mathcal{M})$ and \mathcal{S} is minimized [4].

$$D(\mathcal{T}(\mathcal{M}), \mathcal{S}) := \sum_{\mathbf{m} \in \mathcal{T}(\mathcal{M})} \sum_{\mathbf{s} \in \mathcal{S}} \rho(\mathbf{m} - \mathbf{s}), \quad (1)$$

where $\rho(\cdot)$ is a general objective function, and can be the square of the Euclidean distance combined with the photometric error. ICP and its variants are the most commonly used point set registration algorithms, but they cannot guarantee the global minimum of the cost function (1) [22].

Feature-based and direct methods are also the examples of iterative SLAM. They try to minimize the reprojection or photometric error to estimate the pose transformation. Assume that the perspective model $\pi_p(\cdot)$ projects 3-D point \mathbf{p}_i to image point \mathbf{u}_i , so that $\mathbf{u}_i = \pi_p(\mathbf{E}_{CW} \mathbf{p}_i)$ where \mathbf{E}_{CW} is the transform matrix from the world to camera frame. Incremental poses \mathbf{E}'_{CW} are expressed by left-multiplication a vector μ with 6 DoF based on the exponential mapping, i.e., $\mathbf{E}'_{CW} = \exp(\mu) \mathbf{E}_{CW}$.

In feature-based methods, feature points \mathbf{u}_i in one image are reprojected to another image \mathbf{u}'_i , so that the incremental

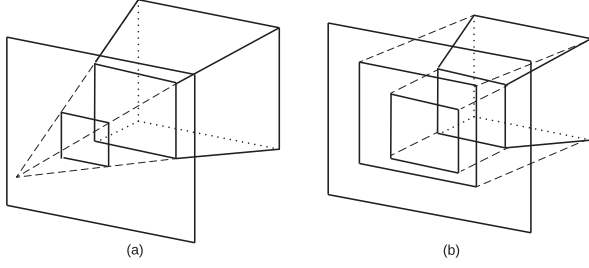


Fig. 2. Differences between perspective and axonometric projections. The perspective projection (a) projects 3-D points on the principle point, while axonometric projection (b) projects points on the axonometric plane. A quadrangular frustum pyramid can be a rectangle when the vertex coincides with the principle point. While for axonometric image, the size ratio of the two rectangles will not change. This simple property is used for data decoupling.

pose transformation vector μ can be estimated by minimizing the reprojection error \mathcal{R} .

$$\mathcal{R}(\mu) := \sum_i \rho(u'_i - \pi_p(\mathbf{E}'_{CW} \pi_p^{-1}(u_i, \mathbf{E}_{CW}))). \quad (2)$$

In [11], where the FAST corner detector is applied, ρ is the Tukey biweight function; whereas in [2], [12], ρ is the L_2 -norm function. For monocular camera, an initial process to obtain the depths of points is needed [11], [13], while for stereo/RGB-D camera, this process can be skipped [45], [46].

In direct methods, new images are aligned with several key frames I_r by minimizing the photometric error \mathcal{H} given in (3). Similar expressions can be found in [12], [14], [17], [18], [47]. Note that the direct RGB-D SLAM [14] also minimizes depth error over all pixels.

$$\mathcal{H}(\mu) := \sum_{i,r} \rho(I_r(u'_i) - I(\pi_p(\mathbf{E}'_{C_rW} \pi_p^{-1}(u_i, \mathbf{E}_{CW}))). \quad (3)$$

Being non-robust to illumination changes is one of the potential problems of matching pixel intensities [18]. Since (2) and (3) are highly non-linear, iterative numerical solutions are needed. Unfortunately, they are sensitive to initialization and cannot guarantee the global optimal solution either.

Iterative solutions also play a significant role in tightly-coupled inertial fusion with the above methods. The inertial residual is imposed into the objective function of ICP (1), reprojection error (2), and photometric error (3), resulting in the RGB-D-inertial [22], reprojection-inertial [21], and direct-inertial [20] optimization problems, respectively. Similar to the above, the iterative numerical solutions are needed.

B. Non-Iterative Framework

The proposed non-iterative framework as shown in Fig. 1 consists of several blocks and will be explained in the Section IV to VIII. In short, a procedure of decoupling-estimation-recoupling is proposed as follows: 3-D point clouds are first decoupled into several subspaces, where data can be matched independently with lower complexity; then the camera motion is obtained from recoupling the estimation in the subspaces. Based on the single key-frame training, the translation of the decoupled 1-D vector is predicted using a kernel cross-correlator (KCC). This enables the fast motion estimation on

ultra low power processors. The 6 DoF pose estimation is recoupled by fusing the inertial measurements with a simple pose estimator. Finally, 3-D maps are fused with non-key-frames by a moving average, so that the missing information of key-frames is complemented with complexity $\mathcal{O}(n)$.

IV. DATA DECOUPLING

This section will introduce the process of point cloud decoupling, from 6 DoF to 1 DoF. As shown in Fig. 1, we are introducing a loop where the first block is dependent on the output of the last block. At the time of beginning, the camera is assumed to be located at the origin.

A. 6 DoF to 3 DoF

It has been shown that even the low-cost, low-precision inertial measurement unit (IMU) can significantly increase performance on the attitude estimation [40]. To avoid the traditional optimization problem and decouple the rotational and translational DoF, the posterior attitude estimation in Section IX that is fused with AHRS is utilized, so that the rotational movements in 3-D space are decoupled from translational movements. This idea of estimation after decoupling is proved to be feasible in [48], which leverages on orientation histograms for roughly attitude estimation. However, it requires a fine alignment in the final step by running ICP and the translation estimation is based on the linear correlation by 3-D Fourier transform with complexity $\mathcal{O}(n_x n_y n_z \log n_x n_y n_z)$, where n_x, n_y, n_z are the number of voxels in each dimension, respectively. The proposed method is based on the kernel correlation and only with complexity $\mathcal{O}(n \log n)$, where $n = n_x n_y$ is the number points after axonometric projection. A point cloud is a set of points with pose $\mathbf{G} \in \mathbf{SE}(3)$ and is defined with a specified color to represent an external surface of an object or environment. Assume the k_{th} key-frame is denoted as $\mathcal{K}_k(\mathbf{G}_k)$, a point cloud $\mathcal{P}_i(\mathbf{G}_i)$ can be rotated to align with the key-frame by its orientation $\mathbf{R}^+ \in \mathbf{SO}(3)$ where the superscript $+$ denotes the posterior estimation, so that the aligned point cloud $\tilde{\mathcal{P}}_i$ can be obtained through

$$\tilde{\mathcal{P}}_i(\mathbf{t}_i) = \mathbf{R}_k^+(\mathbf{R}_i^+)^{-1} \mathcal{P}_i(\mathbf{G}_i^+), \quad (4)$$

where

$$\mathbf{G}^+ = \begin{bmatrix} \mathbf{R}^+ & \mathbf{t}^+ \\ \mathbf{0} & 1 \end{bmatrix} \text{ with } \mathbf{R}^+ \in \mathbf{SO}(3) \text{ and } \mathbf{t}^+ \in \mathbb{R}^3. \quad (5)$$

In this sense, the original 6 DoF \mathbf{G}_i is reduced to 3 translational DoF \mathbf{t}_i , so that from now on, we only need to estimate the translation of the two point clouds \mathcal{P}_i and \mathcal{K}_k .

B. 3 DoF to 2 DoF

Computation requirements can be further reduced if the 3-D translational movements can be decoupled into 3 independent axes. The principle is that the geometry properties in the 3 axes must be kept. We propose to apply axonometric projection on the aligned point cloud $\tilde{\mathcal{P}}_i(\mathbf{t}_i)$ to get axonometric color and depth image $I^C, I^D \in \mathbb{R}^{M \times N}$. A 3-D point $\mathbf{p} = (x, y, z)^T \in \mathcal{P}$ on the visible scene surface is mapped to image coordinates

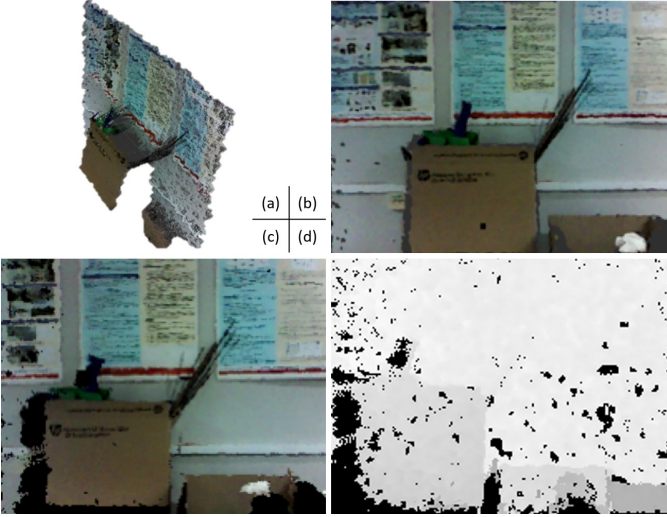


Fig. 3. A point cloud (a) captured by a depth camera is rectified by the posterior attitude estimation. Image (b) is a perspective image. It is reprojected to an axonometric color image (c) and depth image (d). Black holes can be seen in (c) and (d), since some invisible points in (b) are also projected to the axonometric image plane.

$\mathbf{u} = (u, v)^T \in \Omega$ through the axonometric projection model $\pi_a : \mathbb{R}^3 \mapsto \mathbb{R}^2$ defined as:

$$\begin{bmatrix} u \\ v \end{bmatrix} = \frac{1}{r_k} \begin{bmatrix} x \\ y \end{bmatrix}_{\tilde{c}}, \quad (6)$$

where $r_k \in \mathbb{R}^+$ is the projection resolution that can be set adaptively. The subscript \tilde{c} denotes that the point coordinates are expressed in the aligned camera frame. The axonometric depth image is defined as:

$$I^D(\mathbf{u}) = [z]_{\tilde{c}}, \quad (7)$$

which stores the point distances to the axonometric plane versus the perspective depth image that stores the distances to the principle point. The differences between perspective projection and axonometric projection are illustrated in Fig. 2. The perspective projection does not keep the geometric relationship since an object becomes smaller as its distance from the viewpoint increases, while in axonometric projection, the original size of an object is kept. This property decouples the original 3-D translation into the 2-D translation on the axonometric plane and 1-D translation perpendicular to the plane. Therefore, instead of estimating the movements in 3-D space, we can now estimate the 2-D translation of the axonometric images followed by 1-D depth translation estimation.

Before that, one thing that needs to be considered is the projection resolution r_k which is physically the size of covered space by each pixel. The field of view of axonometric projection is a cuboid space with the central axis coinciding with the camera optical axis. Its covered space is determined by the image size $M \times N$ and the projection resolution r_k . Since points outside of the cuboid will be cropped, r_k is needed to be set large enough to make the cuboid cover most of the points. Meanwhile, there will be a large black margin on the image, if r_k is set too large, since not all the pixels can be covered by the projecting points. Moreover, the minimum cuboid envelope

Algorithm 1: Pseudocode for Finding Adaptive r_k

Input : Sampled Point Cloud \mathcal{K}'_k
Output: Adaptive Resolution r_k

- 1 Axonometric Image Size S
- 2 Cuboid $c_i \in \mathcal{C}$; /* \mathcal{C} is the candidates set that are calculated from image size S */
- 3 $c_i.\text{num} \leftarrow 0$
- 4 **for** point \mathbf{p}_j in \mathcal{K}'_k **do**
- 5 find minimum Cuboid $c_i \in \mathcal{C}$ that contains \mathbf{p}_j
- 6 $c_i.\text{num} \leftarrow c_i.\text{num} + 1$
- 7 $c \leftarrow \arg \min_{c_i} \{c_i | c_i.\text{num} \geq 0.8 * |\mathcal{K}'_k|, c_i \in \mathcal{C}\}$
- 8 $r_k \leftarrow c/S$

of a point cloud may change dramatically because of the camera movements. To be robust to the changing scenes, we implement a searching procedure listed in Algorithm 1 to set resolution r_k adaptively. Since most of the boundary points of a point cloud are outliers, algorithm 1 tries to find the cuboid envelope that covers 80% (set empirically) points in the cloud. To be more efficient, it traverses a point cloud by sampling one point in every 25 points. Note that in this process, we keep the central axis of the cuboid envelope coincided with the camera's optical axis. Although the sampling is not precise, we find that the approximation is acceptable and the cost is deserved, since its complexity is only $\mathcal{O}(n/25)$, so that the computational time of Algorithm 1 can even be ignored compared to the calculation in the following sections. To further reduce repeated computation, r_k is updated by r_{k+1} only when the key-frame \mathcal{K}_{k+1} is created. Hence, all the clouds $\tilde{\mathcal{P}}_i$ acquired between \mathcal{K}_k and \mathcal{K}_{k+1} are projected with the resolution r_k and registered with the key-frame \mathcal{K}_k . Another advantage of adaptive resolution is that when the camera is near to the scene surfaces, more details of the scenes are preserved with smaller r_k .

Since the point clouds are generated by pinhole cameras, when they are reprojected on the axonometric plane, some black holes may appear inside the image. This is because some invisible points for pinhole cameras are also projected on the axonometric plane. However, these black holes can be filled by the map fusion process which will be presented in Section VIII. Fig. 3 shows an example that a 6 DoF point cloud is rectified and then reprojected to axonometric images.

C. 2 DoF to 1 DoF

To estimate the translation of two axonometric images, we need to find the translation of their maximum overlap. To this end, we further decouple the axonometric image into a 1-D vector. Let an image $I = [I_{(0)}, I_{(1)}, \dots, I_{(M-1)}]^T \in \mathbb{R}^{M \times N}$, where $I_{(i)}^T \in \mathbb{R}^N$ is the i_{th} row of I , its expanded 1-D vector $\mathbf{x} \in \mathbb{R}^{MN}$ can be defined through an expanding operator $\mathbf{x} = \Psi(I)$, where $\Psi : \mathbb{R}^{M \times N} \mapsto \mathbb{R}^{MN}$ is a bijective function on the condition that the matrix size (M, N) is known:

$$\Psi \left([I_{(0)}, \dots, I_{(M-1)}]^T \right) = [I_{(0)}^T, \dots, I_{(M-1)}^T]^T. \quad (8)$$

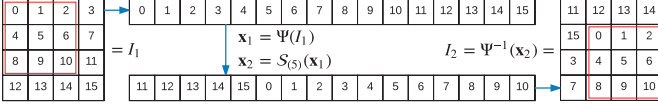


Fig. 4. The axonometric image I_1 are expanded into a 1-D vector $\mathbf{x}_1 = \Psi(I_1)$, and 2-D translation of an image $S_{(x,y)}(I_1)$ can be mapped to a unique circular shift of 1-D vector $S_{(m)}(\mathbf{x}_1)$. In this example, $N = 4$, $M = 4$, the matrix after translation $I_2 = S_{(x,y)}(I_1)$ can be obtained by substituting $m = 5$ into (10), hence $x = 1$, $y = 1$. The elements outside of the maximum overlap (bounded by the red rectangle) contribute nothing for finding translation, hence the malposition of these elements is ignored.

Define the vector's circular shift operator $S_{(m)}(\mathbf{x}) : \mathbb{R}^{MN} \mapsto \mathbb{R}^{MN}$, where $m \in [0, MN-1]$ denotes the operator that circular shifts m elements for \mathbf{x} , then the matrix's translation with (x, y) elements is defined as $S_{(x,y)}(\cdot) : \mathbb{R}^{M \times N} \mapsto \mathbb{R}^{M \times N}$,

$$S_{(x,y)}(I) := \Psi^{-1}(S_{(m)}(\Psi(I))) \quad (9)$$

where

$$x = \begin{cases} (m+1)/N & \text{if } (m+1)/N \leq \frac{M}{2} \\ (m+1)/N - M & \text{else} \end{cases} \quad (10a)$$

$$y = \begin{cases} m\%N & \text{if } m\%N \leq \frac{N}{2} \\ m\%N - N & \text{else} \end{cases} \quad (10b)$$

The definition of matrix translation in (9) is slightly different from our intuitive understanding. For the clarity of the presentation, an intuitive explanation is illustrated in Fig. 4 where 2-D translation of a matrix can be regarded as a unique 1-D circular shift of its expanded vector. A side effect caused by definition (9) is the malposition of the elements outside of the maximum overlap. However, those elements contribute nothing for finding the translation, so that they can just be ignored. In practice, the expanding operation $\Psi(\cdot)$ and its inverse operator $\Psi^{-1}(\cdot)$ do not need to be implemented, since a dense matrix or an image is always stored as its expanding vector in the computer memory. The only thing we need to do is to reinterpret memory through a pointer, hence the complexity of decoupling the translation of an axonometric image is $\mathcal{O}(1)$. From now on, the problem becomes finding the 1-D translation of vectors according to the maximum overlap.

V. SINGLE KEY-FRAME TRAINING

We propose to apply a non-linear cross-correlator to predict the vector translation. Cross-correlators or correlation filters are widely used for object tracking [30], [49] but have not been used for data association in SLAM problem. The correlator used in this paper is based on our previous work kernel cross-correlator (KCC) [31], hence we will only give a short description. The axonometric key-frame and non-key-frames will be denoted as column vectors $\mathbf{z}^{\mathcal{C}, \mathcal{D}}, \mathbf{x}^{\mathcal{C}, \mathcal{D}} \in \mathbb{R}^n$, where the superscript \mathcal{C}, \mathcal{D} denotes the color and depth images and will be left out in the absence of a little ambiguity.

The convolution theorem states that the correlation operation becomes element-wise conjugate multiplication in Fourier domain. Denote the fast Fourier transformation (FFT) $\mathcal{F}(\cdot)$ on a vector as $\hat{\cdot}$, i.e. $\hat{\mathbf{x}} = \mathcal{F}(\mathbf{x})$, so that the cross-correlation of two vectors $\mathbf{g} = \mathbf{x} * \mathbf{h}$ is equivalent to $\hat{\mathbf{g}} = \hat{\mathbf{x}} \odot \hat{\mathbf{h}}^*$,

where the operator \odot and superscript $*$ denote the element-wise multiplication and complex conjugate, respectively. The bottleneck of this operation is to compute the forward and backward FFTs, hence the complexity of the entire process has an upper bound $\mathcal{O}(n \log n)$ where n is the number of elements in the vector. Define the non-linear feature mapping function $\varphi : \mathbb{R}^n \mapsto \mathbb{R}^d$, where $d \gg n$, the kernel trick is to find the inner product of feature mapping without calculating the high dimension features explicitly. Define the kernel function as $\kappa : \mathbb{R}^n \times \mathbb{R}^n \mapsto \mathbb{R}$, such that $\kappa(\mathbf{x}_i, \mathbf{x}_j) = \varphi(\mathbf{x}_i)^T \varphi(\mathbf{x}_j)$. Given a test image $\mathbf{x} \in \mathbb{R}^n$ and its desired correlation output $\mathbf{g} \in \mathbb{R}^m$, the kernel cross-correlator is defined as:

$$\hat{\mathbf{g}} = \hat{\kappa}_{\mathbf{z}}(\mathbf{x}) \odot \hat{\mathbf{h}}^*, \quad (11)$$

where $\kappa_{\mathbf{z}}(\mathbf{x})$ is the kernel vector and is defined as $[\kappa(\mathbf{x}, \mathbf{z}_0), \dots, \kappa(\mathbf{x}, \mathbf{z}_{m-1})]^T$ where $\mathbf{z}_i \in \mathcal{T}(\mathbf{z}) \in \mathbb{R}^n$ is generated from training sample \mathbf{z} , which is the key-frame in this paper. The transform function $\mathcal{T}(\cdot)$ is predefined to imply the training objective and is set as the circular shift $S_{(m)}(\cdot)$ defined in the last section. Note that the length of filter \mathbf{h} and correlation target \mathbf{g} is related to the number of sample-based vector \mathbf{z}_i , i.e. $\mathbf{h}, \mathbf{g} \in \mathbb{C}^m$. The correlation output is transformed back into the spatial domain using the inverse FFT. When a set of training samples \mathbf{z}^i and their associated training outputs \mathbf{g}^i are given, the objective is to find a filter \mathbf{h} to satisfy (11). Normally, \mathbf{g}^i can take any shape and will be discussed later. Training is conducted in the Fourier domain to take advantage of the simple element-wise operation between the input and output. A similar technique is also used in [49] which proposes a linear correlation filter, while the proposed method extends it to the kernel space. To find the filter \mathbf{h} that maps training inputs to the desired outputs, the sum of squared error (SSE) between the correlation output and the desired output in frequency domain is minimized:

$$\min_{\hat{\mathbf{h}}^*} \sum_i \|\hat{\kappa}_{\mathbf{z}^i}(\mathbf{z}^i) \odot \hat{\mathbf{h}}^* - \hat{\mathbf{g}}^i\|^2 + \lambda \|\hat{\mathbf{h}}^*\|^2, \quad (12)$$

where the second term is a regularization to prevent over fitting. Solving the optimization problem (12) requires setting zero to the first derivative of filter $\hat{\mathbf{h}}^*$,

$$\frac{\partial}{\partial \hat{\mathbf{h}}^*} \left(\sum_i \|\hat{\kappa}_{\mathbf{z}^i}(\mathbf{z}^i) \odot \hat{\mathbf{h}}^* - \hat{\mathbf{g}}^i\|^2 + \lambda \|\hat{\mathbf{h}}^*\|^2 \right) = 0. \quad (13)$$

Since all the operations in (13) are performed in element-wise, the elements of $\hat{\mathbf{h}}^*$ can be found independently, and a closed-form solution can be obtained:

$$\hat{\mathbf{h}}^* = \frac{\sum_i \hat{\mathbf{g}}^i \odot \hat{\kappa}_{\mathbf{z}^i}^*(\mathbf{z}^i)}{\sum_i \hat{\kappa}_{\mathbf{z}^i}(\mathbf{z}^i) \odot \hat{\kappa}_{\mathbf{z}^i}^*(\mathbf{z}^i) + \lambda}, \quad (14)$$

where the operator \div denotes the element-wise division. More specifically, we assume that only one key-frame $\mathbf{z} \in \mathbb{R}^n$ is available, hence the summation for the number of training samples \mathbf{z}^i can be left out, resulting in a compact formula,

$$\hat{\mathbf{h}}^* = \frac{\hat{\mathbf{g}}}{\hat{\kappa}_{\mathbf{z}}(\mathbf{z}) + \lambda}. \quad (15)$$

The pattern of translational motion of the key-frame \mathbf{z} is learnt and stored in the filter \mathbf{h} . In the experiments, the radial-basis kernel (16) is used for calculating the kernel vector $\hat{\kappa}_{\mathbf{z}}(\mathbf{x})$.

$$\kappa(\mathbf{x}, \mathbf{z}_i) = h(\|\mathbf{x} - \mathbf{z}_i\|^2). \quad (16)$$

To compute the kernel vector efficiently, we first expand the norm in (16):

$$h(\|\mathbf{x} - \mathbf{z}_i\|^2) = h(\|\mathbf{x}\|^2 + \|\mathbf{z}_i\|^2 - 2\mathbf{x}^T \mathbf{z}_i). \quad (17)$$

Since $\|\mathbf{x}\|^2$ and $\|\mathbf{z}_i\|^2$ are constant, the kernel vector can be calculated as:

$$\kappa_{\mathbf{z}}(\mathbf{x}) = [h(\|\mathbf{x} - \mathbf{z}_1\|^2), \dots, h(\|\mathbf{x} - \mathbf{z}_n\|^2)]^T \quad (18a)$$

$$= h(\|\mathbf{x}\|^2 + \|\mathbf{z}\|^2 - 2[\mathbf{x}^T \mathbf{z}_1, \dots, \mathbf{x}^T \mathbf{z}_n]^T). \quad (18b)$$

From the correlation theory, $\mathbf{x} * \mathbf{z} = [\mathbf{x}^T \mathbf{z}_1, \dots, \mathbf{x}^T \mathbf{z}_n]^T$, since \mathbf{z}_i are the circular shifts of \mathbf{z} . Substitute it into (18b),

$$\kappa_{\mathbf{z}}(\mathbf{x}) = h(\|\mathbf{x}\|^2 + \|\mathbf{z}\|^2 - 2 \cdot \mathbf{x} * \mathbf{z}) \quad (19a)$$

$$= h(\|\mathbf{x}\|^2 + \|\mathbf{z}\|^2 - 2 \cdot \mathcal{F}^{-1}(\hat{\mathbf{x}} \odot \hat{\mathbf{z}})). \quad (19b)$$

The bottle-neck of (19b) is the forward and backward FFTs, so that the kernel vector can be calculated in complexity $\mathcal{O}(n \log n)$. For implementation purpose, the vector norm in (19b) is obtained in frequency domain using Parseval's theorem, so that the original signals don't need to be stored.

$$\kappa_{\mathbf{z}}(\mathbf{x}) = h\left(\frac{1}{n}\|\hat{\mathbf{x}}\|^2 + \frac{1}{n}\|\hat{\mathbf{z}}\|^2 - 2 \cdot \mathcal{F}^{-1}(\hat{\mathbf{x}} \odot \hat{\mathbf{z}}^*)\right). \quad (20)$$

VI. TRANSLATION ESTIMATION

Based on the single key-frame training, the translational pattern of a new axonometric image can be estimated directly by regarding the new frame as a test sample.

A. Image Translation Estimation

To make the correlation output more distinctive, \mathbf{g} is set as a binary vector, such that the single peak is located at the first element, i.e. $g_{[0]} = 1$, where the bracket $[\cdot]$ is used for accessing the element with index (starting from 0). The explanation is that, after computing a kernel correlation for a test image in the Fourier domain and converting back to the spatial domain, the shift output of value 1 will correspond to the shift of the test sample. Because of the noises and occlusion, it is nearly impossible to get the exact peak value 1. Instead, the location of the maximum value can be used to indicate the translation \tilde{m} of the test images.

$$\tilde{m} = \arg \max_i \underbrace{\mathcal{F}^{-1}(\hat{\kappa}_{\mathbf{z}}(\mathbf{x}) \odot \hat{\mathbf{h}}^*)}_{\mathbf{g}_{[i]}(\mathbf{x})} \quad (21)$$

Substitute (21) into (10) and multiply the adaptive resolution r_k , the predicted translation $[\mathbf{t}_{[0]}, \mathbf{t}_{[1]}]^T$ of axonometric image can be obtained:

$$[\mathbf{t}_{[0]}, \mathbf{t}_{[1]}]^T = r_k \cdot [\tilde{x}, \tilde{y}]^T. \quad (22)$$

The complexity of (21) is bounded by the calculation of kernel vector and the inverse FFT of correlation output $\hat{\mathbf{g}}(\mathbf{x})$, hence the image translation estimation $[\mathbf{t}_{[0]}, \mathbf{t}_{[1]}]$ can be obtained with complexity $\mathcal{O}(n \log(n))$.

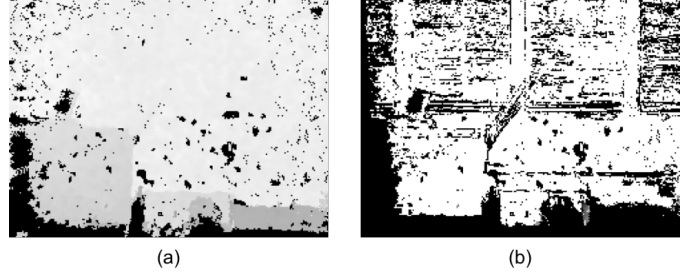


Fig. 5. The left image (a) is an axonometric depth image from Fig. 3. The corresponding well-matched points are shown in the right image (b) by pixel intensities. The higher the brightness, the more confidence the matches have.

B. Depth Translation Estimation

The overlap of axonometric image \mathbf{x} can be matched with key-frame \mathbf{z} , if \mathbf{x} is shifted back with \tilde{m} elements. Inspired by this, the camera motion in the depth direction can be estimated in (23a) which averages the depth differences of the matched pixels. Since not all the pixels are projected by valid points in a cloud, we remove these pixels inside the black holes and only take the points in the set \mathcal{W} defined in (23b) that contains all well-matched pixels.

$$\mathbf{t}_{[2]} = \frac{1}{\#\mathcal{W}} \sum_{i \in \mathcal{W}} (\mathcal{S}_{(-\tilde{m})}(\mathbf{x}_{[i]}^{\mathcal{D}}) - \mathbf{z}_{[i]}^{\mathcal{D}}), \quad (23a)$$

$$\mathcal{W} = \left\{ i \mid \rho(\mathcal{S}_{(-\tilde{m})}(\mathbf{x}_{[i]}^{\mathcal{C}, \mathcal{D}}) - \mathbf{z}_{[i]}^{\mathcal{C}, \mathcal{D}}) < T_{c,d} \right\}, \quad (23b)$$

where the operator $\#$ returns the number of elements in a set and $\rho(\cdot)$ is a general objective function (L_1 -norm in our tests). The predefined thresholds T_c and T_d are designed to eliminate the influence of the dynamic points. This is because dynamic objects naturally cannot be matched with the shifted image $\mathcal{S}_{(-\tilde{m})}(\mathbf{x})$ either in color or depth spaces. Fig. 5 demonstrates an axonometric depth image and its corresponding well-matched points. The advantage of (23) is that it only requires the average differences of depth image which is extremely fast to compute and all the well-matched points are able to contribute to the estimation, making it robust to depth noises. Therefore, the complexity of depth translation estimation is bounded by $\mathcal{O}(n)$. Now, the translation \mathbf{t}_i of the point cloud $\tilde{\mathcal{P}}_i$ relative to the key-frame \mathcal{K}_k is obtained in all three directions based on the decoupled translational motion.

VII. KEY-FRAME SELECTION

As the camera moves, the overlap between the new point cloud and the key-frame may decrease. Hence the peak value may not be distinct enough and new key-frame is needed to ensure large overlap. Since all the new point clouds are matched with key-frames, estimated error will be accumulated when a new key-frame is created. Although loop closure is able to reduce such accumulated error, it needs the camera to revisit a location which can not always happen. Therefore, it is needed to be very careful to create a new key-frame. There are some useful works doing this. For example, DVO [14] uses the logarithmic determinant of the error distribution covariance matrix to determine when to create a new key-frame. PTAM [11] created several conditions for inserting new

key-frames: the distance to the last key-frame is large enough; at least twenty key-frames are passed. ORB-SLAM [13] added new conditions: imposing a minimum visual change based on the percentage of tracked features. However, these conditions are added in an ad-hoc way, and may not be suitable for all scenarios. For example, when the camera moves very fast, the condition of passed twenty frames may prevent creating enough key-frames and will make the camera lose tracking easily. Also, when the motion is gentle, there may be too many key-frames which are not necessary. Therefore, we argue that the condition for creating new key-frames should not be relevant to the number of passed frames and the maximum overlap or the percentage of tracked features but should be able to represent the matching quality. On the other hand, the overlap of two frames may not be proportional to the matching quality because of the existence of dynamic objects, etc. Considering the computational cost, we propose to apply a very simple criterion, i.e. peak to sidelobe ratio (PSR) [49] $P_{sr} : \mathbb{R}^n \mapsto \mathbb{R}$ which is a measurement of peak strength. In this criterion (24), the correlation output $\mathbf{g}(\mathbf{x})$ is split into the peak which is the maximum value and the sidelobe which is the rest of pixels excluding the peak:

$$P_{sr}(\mathbf{x}) = \frac{\max \mathbf{g}_{[i]}(\mathbf{x}) - \mu_s}{\sigma_s} < T_K, \quad (24)$$

where μ_s and σ_s are the mean and standard deviation of the sidelobe. A straightforward explanation is that the peak strength of the correlation output $\mathbf{g}(\mathbf{x})$ indicates the matching confidence level. The desired output with single peak has infinite peak strength. $P_{sr}(\mathbf{x})$ is regarded as a trigger to insert a new key-frame \mathbf{x} into map when it is smaller than T_K . The criterion (24) is not only able to control the minimum confidence of each matching, but also save computational time, especially when the camera is kept still or moving slowly since there is no new training data is required. Only the calculation of mean and standard deviation of the sidelobe are performed in (24), hence the complexity of computing $P_{sr}(\mathbf{x})$ is $\mathcal{O}(n)$.

VIII. MAP REFINEMENT AND FUSION

To reduce the computational requirements, only the key-frames are selected to represent a map. As mentioned earlier, not all the pixels of axonometric images can be reprojected by valid points, and some black holes may appear. A very simple idea is to complement the missing information of the key-frame \mathbf{z} by the non-key-frames \mathbf{x}_k that are already matched with the key-frame \mathbf{z} . This is useful especially when the camera is kept still or moving slowly, since the criterion (24) for creating new key-frame is often not satisfied, and all those new frame \mathbf{x}_k can be used to refine the key-frame \mathbf{z} . Defining the weights vector $\mathbf{w} \in \text{Dom}(\mathbf{z})$, we propose to refine the key-frame $\mathbf{z}^{c,D}$ by the moving average in (25) which is performed in both color and depth spaces.

$$\mathbf{s}_k \leftarrow \mathbf{w}^z + \mathcal{S}_{(-\tilde{m})}(\mathbf{w}_k^x) + e, \quad (25a)$$

$$\mathbf{z}^c \leftarrow (\mathbf{w}^z \odot \mathbf{z}^c + \mathcal{S}_{(-\tilde{m})}(\mathbf{w}_k^x \odot \mathbf{x}_k^c)) / \mathbf{s}_k, \quad (25b)$$

$$\mathbf{z}^D \leftarrow (\mathbf{w}^z \odot \mathbf{z}^D + \mathcal{S}_{(-\tilde{m})}(\mathbf{w}_k^x \odot (\mathbf{x}_k^D - \mathbf{t}_{[2]}))) / \mathbf{s}_k, \quad (25c)$$

$$\mathbf{w}^z \leftarrow \mathbf{w}^z + \mathcal{S}_{(-\tilde{m})}(\mathbf{w}_k^x), \quad (25d)$$

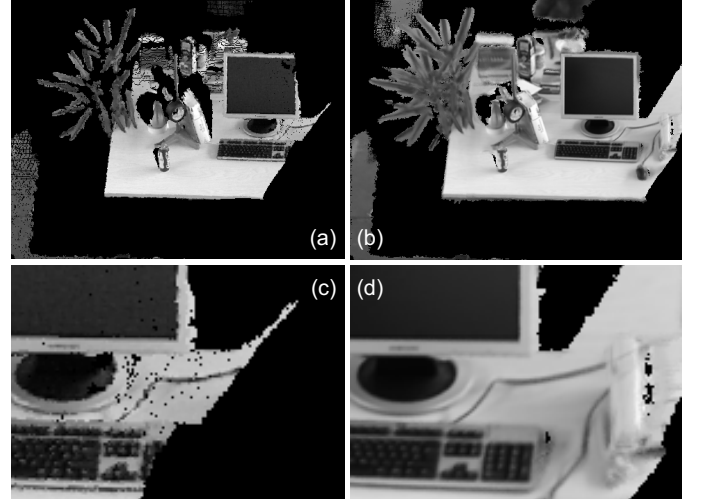


Fig. 6. (a) is a new key-frame. (b) is the refined key-frame during run time. Tests show that the “black holes” in the original axonometric image can be filled by subsequent matched images based on (25). (c) and (d) are the same part of the new and refined key-frame in (a) and (b), respectively. Note that the keyboard is nearly perfectly complemented. The moving average operation will not make it blurred, if the image translation is estimated correctly.

where e is a small scalar (set as $1e^{-7}$) to prevent division by 0. The elements of the weights vector $\mathbf{w} \in \mathbb{R}^n$ present the weight of the corresponding pixel to be fused. Each time a frame \mathbf{x}_k is acquired, its corresponding weight vector \mathbf{w}_k^x is initialized as $\mathbf{w}_{k[i]}^x \leftarrow \{0, 1\}$ where 1 or 0 indicates whether the pixel $\mathbf{x}_{[i]}$ can be seen in the original point cloud or not. This initialization is performed together with the procedure of axonometric reprojection. When the frame \mathbf{x}_k is selected as a new key-frame, the weights vector \mathbf{w}^z is initialized by the weight vector of that frame, i.e. $\mathbf{w}^z \leftarrow \mathbf{w}_k^x$.

Because of the dynamic points and outliers, some valid points in the key-frame \mathbf{z} can not be matched with \mathbf{x}_k . Hence, we remove the unmatched points before (25) is performed. To this end, the pixels of \mathbf{w}_k^x corresponding to those points are set as 0 in (26), so that they can not be fused into the key-frames.

$$\mathbf{w}_{k[i]}^x \leftarrow 0, \text{ if } i \notin \mathcal{W}, \quad (26)$$

where the set \mathcal{W} is defined in (23b) that contains all matched points indexes. To obtain higher quality map, (25) is performed only when $P_{sr}(\mathbf{x}_k) > T_M$ where T_M is the a threshold to control the confidence of map fusion and normally $T_M > T_K$. Since all the operations in (25) are element-wise, the complexity of map refinement process is $\mathcal{O}(n)$. Fig. 6 illustrates an example that a key-frame is refined by its subsequent frames. It demonstrates that the missing information of key-frames can be complemented and many details are able to be preserved.

IX. POSE ESTIMATION AND DATA RECOUPLING

To simplify the estimation process, we propose to fuse the inertial measurements from the AHRS by loosely coupled methods. As mentioned in Section II, AHRS consists of sensors on three axes and is equipped with on-board processing unit to provide superior reliable attitude information. Since the gyroscope and acceleration biases are complemented in

the AHRS system, the state vector is only composed of the sensor position $\mathbf{t} \in \mathbb{R}^3$ in the inertial world frame, its velocity $\mathbf{v}_\omega \in \mathbb{R}^3$ and attitude represented by quaternion \mathbf{q}_ω . This yields a 10-element state vector $\mathbf{X} = [\mathbf{q}_\omega^T, \mathbf{t}^T, \mathbf{v}_\omega^T]^T$ and a simple kinetic model [50] can be established.

To derive the covariance for translation estimation defined in (22), the correlation output $\Psi^{-1}(\mathbf{g}(\mathbf{x}))$ is approximated by Gaussian distribution, which is first proposed in our previous work [51]. Intuitively, the value of each element $\Psi_{[i,j]}^{-1}(\mathbf{g}(\mathbf{x}))$ indicates the estimated confidence of the corresponding image translation (i, j) . Hence the estimated covariance can be found by calculating the covariance of weighted relative translation to the peak. However, its complexity is $\mathcal{O}(n)$. To reduce the computation, it is assumed that the normalized correlation output $\Psi^{-1}(\mathbf{g}(\mathbf{x}))/\sum \mathbf{g}(\mathbf{x})$ is a 2-D Gaussian mask with the center on the peak. Since the peak value of a 2-D Gaussian function is $1/(2\pi\sigma_i\sigma_j)$, where σ_i, σ_j are the standard deviation, the estimated covariance $\sigma_{\mathbf{p}[0]}^2, \sigma_{\mathbf{p}[1]}^2$ in the axonometric plane can be approximated with complexity $\mathcal{O}(1)$:

$$\sigma_{\mathbf{p}[0]}^2 = \sigma_{\mathbf{p}[1]}^2 = \frac{r_k^2 \cdot \sum \mathbf{g}(\mathbf{x})}{2\pi \cdot \max \mathbf{g}_{[i]}(\mathbf{x})}, \quad (27)$$

where the maximum value of $\mathbf{g}_{[i]}(\mathbf{x})$ is already found in (21) and r_k is the projection resolution defined in Algorithm 1. Note that it is not necessary to calculate the summation $\sum \mathbf{g}(\mathbf{x})$ in complexity $\mathcal{O}(n)$, since the mean value of the sidelobe μ_s is calculated in (24), so that $\sum \mathbf{g}(\mathbf{x}) = (n-1)\mu_s + \max \mathbf{g}_{[i]}(\mathbf{x})$. Fig. 7 presents some examples of the correlation output, which shows that it can be approximated by a Gaussian mask especially when $P_{sr}(\mathbf{x}) > 20$, since $T_M > T_K > 20$, this approximation can be safely used. The estimated variance in depth translation can be obtained through direct calculation:

$$\sigma_{\mathbf{p}[2]}^2 = \text{Var}_{i \in \mathcal{W}} \left(\mathcal{S}_{(-\bar{m})}(\mathbf{x}_{[i]}^{\mathcal{D}}) - \mathbf{z}_{[i]}^{\mathcal{D}} \right). \quad (28)$$

where point set \mathcal{W} is defined in (23b). Since the estimation in the three translational subspaces are decoupled and assumed to be independent, the translation covariance $\sigma_{\mathbf{p}}$ is a diagonal matrix and $\sigma_{\mathbf{p}}^2 = \text{diag}(\sigma_{\mathbf{p}[0]}^2, \sigma_{\mathbf{p}[1]}^2, \sigma_{\mathbf{p}[2]}^2)$. Now based on the simple Kalman filter, we are able to recouple the movements to the original 3-D space. Bounded by the key-frame training and translation estimation, the overall complexity is $\mathcal{O}(n \log n)$.

X. EXPERIMENTAL RESULTS

Throughout this paper, a set of algorithms to decrease the computational requirements for the front-end of SLAM system have been developed. They compose the basic components of the proposed non-iterative framework. We will evaluate the system both quantitatively and qualitatively in terms of trajectory estimation, runtime efficiency and dense mapping on low power system and extreme conditions such as fast motion, dynamic scenes, and featureless environments.

A. Implementation

In all the experiments, the Gaussian kernel function is used with standard deviation 0.2 pixels. The regularization term λ in solution (14) and (15), the matching difference threshold

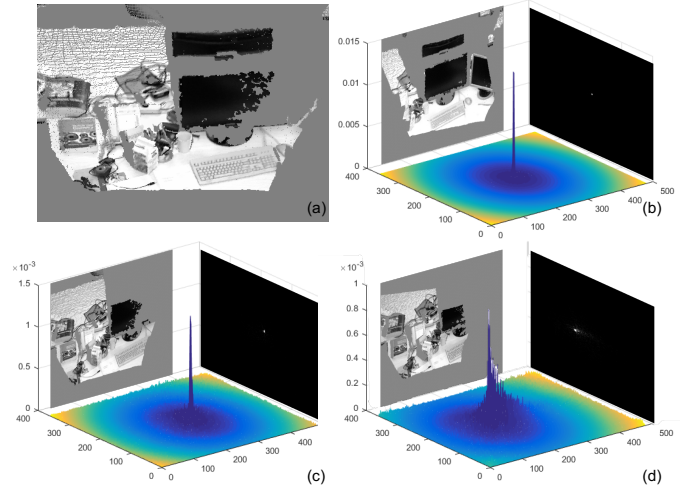


Fig. 7. The examples of the correlation output from a sequence. (a) is the first key-frame; the figure (b), (c), and (d) are the 10_{th} , 43_{th} and 188_{th} frames respectively. Their correlation outputs are shown on the top-right of the corresponding figures whose PSR is 161, 71, and 41 respectively. For better visualization, the outputs are normalized and shown in 3-D space. We find that they can be approximated by 2-D Gaussian functions with the centre on the peak. This assumption is used for computing the covariance in (27).

T_c and T_d for color and depth images are all set as 0.1. In experiments, we found these parameters are not sensitive to the test environments, since different scenarios and sensors are tested and the results are not much affected by different choices of these parameters. The PSR thresholds for creating new key-frame T_K and the condition for map fusion T_M are set as 50 and 100 respectively. Fig. 8 presents the changing of PSR value as the first 200 frames from the same dataset as Fig. 7. It can be seen that when the matching confidence is lower than T_K , a new key-frame will be created so that the matching confidence returns back to high position.

To test the performance of the proposed framework on ultra-low power processors and compare with the state-of-the-art algorithms, two different platforms are used. One is the credit card sized UpBoard[®] that is equipped with an ultra-low power mobile-phone-level processor Atom x5-Z8350 with scenario design power 2W. Running at 1.44GHz with 2G RAM, this platform is very difficult for most of the state-of-the-art algorithms to run in real-time. Therefore, for comparison and visualization purpose, the framework is also tested on a standard PC running Ubuntu 16.04 with an Intel Core i7-4700 CPU and 8G RAM. Limited by the payloads and power consumption, we choose Intel RealSense[®] camera to work with the UpBoard[®], and Microsoft Kinect[®] to work with the standard PC. Both cameras are integrated with an inertial sensor, myAHRS+¹, which is a low cost high performance AHRS containing a 16-bit 3-axis gyroscope, a 16-bit 3-axis accelerometer, and a 13-bit 3-axis magnetometer.

B. Real-Time Performance on Depth Cameras

Real-time trajectory estimation using depth camera is demonstrated and compared with the other state-of-the-art

¹https://github.com/wang-chen/myahrs_driver

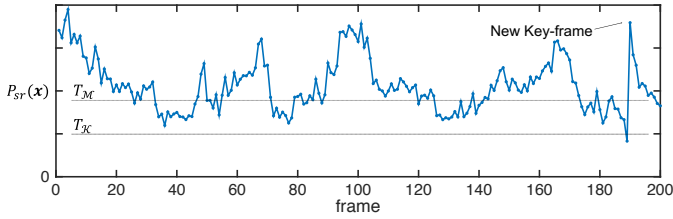


Fig. 8. The first 200 frames of the sequence in Fig. 7 are extracted to show the tendency of PSR with respect to frames number. Only when the PSR of the correlation output goes below T_K , a new key-frame will be selected. The point clouds will be fused with the key-frames when PSR is higher than T_M .

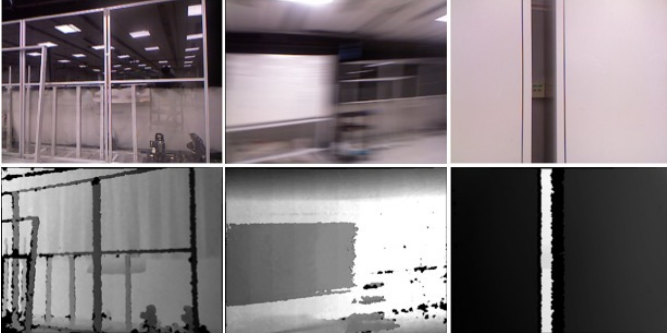


Fig. 9. The examples of color (up) and depth (down) images of the testing area. This datasets are quite challenging for vision-based SLAM methods, since lots of specular reflections, motion blur, and featureless regions can be seen. However, the proposed method works well in this situation.

methods, RGB-D SLAM2 [19], ElasticFusion [8], and ORB-SLAM2 (RGB-D) [13], [52]. All the reported performances are based on their open source implementation on robot operating system (ROS) using the root mean squared error (RMSE), absolute mean error (MEAN), and median absolute error (MAE). Although these methods provide no inertial fusion, they are still excellent benchmarks for comparison, since they have been extensively tested by the robotics community. The open implementation of other RGB-D-inertial dense mapping methods such as [22] is unavailable, hence we are unable to compare with them. Since ElasticFusion does not provide ROS interface, a ROS wrapper is implemented to receive images through ROS communication protocol. Some of the above methods optimize the whole trajectory in the back-end, and output the optimized trajectory only after the program is terminated. This is not suitable for low-latency robotic systems. To evaluate and compare real-time performance, only the instant pose estimation is accepted.

The experiment datasets are recorded in an indoor environment equipped with a high accurate Vicon motion capture system which is to provide ground truth. Different traveling distances, speeds, dynamics and illumination conditions are covered. Except for the 6 DoF ground truth, the data include raw measurements from the Kinect at 30Hz, inertial measurements from AHRS at 100Hz. These datasets are released and can be downloaded² for research purpose. Some of the examples of the recorded color and depth images can be found in Fig. 9. It is highlighted that they are quite challenging

for vision-based methods because there are lots of specular reflections and featureless regions in the environment.

1) *Performance on High Power Platform:* As can be seen in Table I, the proposed method achieves best performance on the PC platform. We notice that the accuracy of feature-based methods, ORB-SLAM2 and RGB-D SLAM2 vary a lot in different datasets, this may be due to the existence of specular reflection and features-less regions. This phenomenon indicates that the feature-based methods are quite sensitive to feature outliers. It can be compared with ElasticFusion and our method, that have similar pose estimation error for different datasets. The ICP-based method ElasticFusion requires powerful GPU, while our method is based on KCC that is fast and robust to object distortion and occlusion.

The performance of efficiency on the same datasets is shown in Table II, which indicates that the proposed framework outperforms all the other methods in terms of running time (update rate). Note that the running time of our method reported in Table II contains the summation of both tracking and mapping; while that of the other methods only contain the tracking time. This is because the implementation of tracking thread is independent of the local mapping in other methods, while they are processed sequentially in ours with one thread, although they can also be implemented parallelly. The running time varies for different datasets according to the number of trainings. If landmarks change rapidly, our method has to train new models based on new key-frame thus increases a little bit of running time. For ElasticFusion, the reported accuracy is obtained from slowing down the process of sending images 6 times to make sure there is no dropping frames.

We note the high accuracy performance of ORB-SLAM2 in some situations. ORB-SLAM2 is implemented as a full SLAM system with loop closure detection, while our method is an odometry system for which drift is inevitable. Due to this reason, we found that the accuracy performance of ORB-SLAM is better when visual loop closure is available frequently and is good at tracking the environments with lots of visual features. We find that the accuracy of such feature-based methods will drop dramatically in feature-less and pseudo-feature environments, while our KCC-based method is robust to object distortion and occlusion. In this sense, the proposed non-iterative framework provides a new solution for the front-end (data association) of RGB-D-inertial SLAM system, that works well in environments for which traditional methods is not suitable. Similar to ORB-SLAM and also other methods, we can apply the off-the-shelf loop closure detection algorithms, such as DBow2 [53] and OpenFabMap [54], to detect the visual loop and close the loop by G²O [55] to correct both translational and rotational drifts. This will further improve the accuracy performance, but it is out of the scope of this paper, as the main focus is the data association procedure.

2) *Performance on Low Power Platform:* It has been shown that the proposed non-iterative framework requires the least computational resources. Experiments on the Up-Board[®] also show that it may be the only one that can run on the such ultra low power platforms in real-time (30Hz). The average running time of tracking and mapping are listed respectively in Table III, where that of ORB-SLAM2 is also given for comparison.

²https://wang-chen.github.io/ni_slam

TABLE I
REAL-TIME ACCURACY COMPARISON ON THE KINECT DATASET WITH PC PLATFORM.[†]

Dataset	ours			ORB-SLAM2 (RGB-D)			ElasticFusion			RGB-D SLAM2		
	RMSE	MEAN	MAE	RMSE	MEAN	MAE	RMSE	MEAN	MAE	RMSE	MEAN	MAE
01_cir	0.106	0.099	0.092	<u>0.323</u>	0.308	0.348	0.595	0.554	0.462	1.092/0.122	0.434/0.106	0.180/0.087
02_fir	0.373	0.294	0.221	-	-	-	<u>0.602</u>	0.573	0.437	1.069/0.575	<u>0.557</u> /0.397	<u>0.188</u> /0.136
03_rec	0.123	0.110	0.097	<u>0.142</u>	0.118	0.100	0.454	0.389	0.387	1.326/0.191	<u>0.643</u> /0.182	0.294/0.174
04_tri	0.076	<u>0.066</u>	<u>0.058</u>	0.058	0.051	0.045	0.123	0.109	0.092	0.898/0.124	0.365/0.111	0.195/0.101
05_dor	0.093	0.084	0.070	0.513	0.464	0.412	<u>0.281</u>	<u>0.254</u>	0.264	1.243/0.760	0.784/0.691	0.575/0.691
06_rot	0.113	0.103	0.100	<u>0.128</u>	0.114	<u>0.103</u>	0.355	0.327	0.321	1.477/0.543	1.075/0.520	0.925/0.515
07_shk	0.021	0.019	0.017	<u>0.025</u>	0.021	0.013	0.024	0.021	0.020	<u>0.022</u> /0.031	<u>0.020</u> /0.022	<u>0.016</u> /0.016
overall	0.129	0.111	0.094	<u>0.198</u>	0.179	<u>0.170</u>	0.345	0.318	0.279	1.014/0.335	0.554/0.290	0.339/0.246

[†]Bold texts and texts with underscore indicate the best two performance. '-' indicates that method cannot produce an estimation for whole trajectory. The corresponding performance on efficiency is give in Table II. It is noticed that the real-time pose estimation of RGB-D SLAM2 fluctuates much more than its off-line performance, which is also given for comparison.

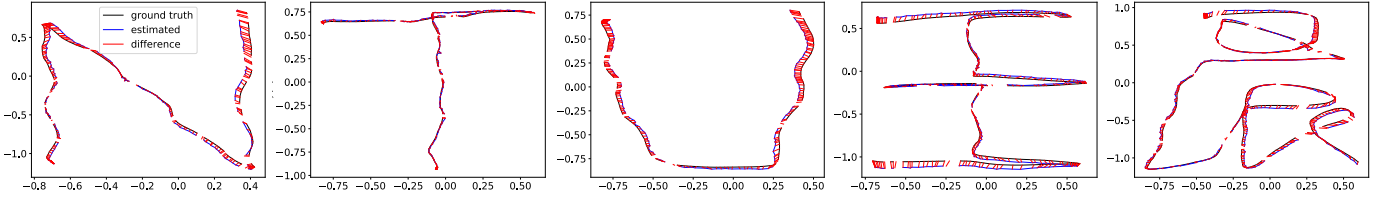


Fig. 10. The trajectory estimation on the low power platform is compared with ground truth. The proposed method is the only one that can run in real-time produce dense maps on this platform. One example of the dense maps produced on the same low power platform is presented in Fig. 11 (a).

TABLE II
REAL-TIME EFFICIENCY COMPARISON ON KINECT DATASET WITH PC PLATFORM. ALL THE DATA ARE GIVE BY AVERAGE UPDATE RATE (Hz).

Datasets	ours	ORB2	EFusion	RGBD2
01_cir	73.4	41.1	5.28	18.7
02_fir	82.2	-	4.72	20.1
03_rec	81.6	41.5	5.34	18.3
04_tri	80.7	45.6	5.99	20.9
05_dor	77.2	42.7	4.58	21.1
06_rot	77.8	46.6	4.57	21.6
07_shk	85.1	50.0	4.67	23.3
overall	79.7	44.6	5.05	20.6

TABLE III
AVERAGE RUNTIME (ms) ON THE ULTRA LOW POWER PLATFORM.[†]

Platform	Method	Tracking	Mapping	Update
Up-Board [®]	ours	26.9	5.4	32.3
	ORB-SLAM2	167	499	≥ 167

[†]All date are tested using RGB-D image with size 640×480 . The mapping process of ORB-SLAM2 is independent with tracking.

Note that ORB-SLAM2 cannot produce and fuse dense maps, while our method takes tracking and dense mapping into one thread and are still able to run in real-time. To the best of our knowledge, the proposed method takes dense mapping to the power-weight-limited micro-robot systems for the first time. Some examples of the overhead trajectory estimation using a downward facing RealSense[®] camera is shown in Fig. 10, which indicates that the proposed method is able to run in real-time and provide accurate trajectory estimation even on the ultra-low power system.

C. Dense Mapping

In this section, we present the qualitative performance of in-door dense reconstruction using depth cameras, i.e., Intel RealSense[®] and Microsoft Kinect[®]. Each camera has its own strengths and weaknesses and can be used for different scenarios. For example, RealSense is light and power efficient, but with limited range measurements, thus it is suitable for indoor objects reconstruction. Fig. 11 (a) shows an example of cubicles reconstruction using RealSense camera. All the point

clouds are processed and fused in real-time on the mobile level processing board UpBoard[®]. Only for visualization purpose, they are sent to a remote server with a screen to display. It can be seen that the point clouds align pretty well and the 3-D map depicts the environment faithfully. It is noticed that there are some small holes in the map of Fig. 11 (a). This is because the structured-light-based cameras are sensitive to the object color and material; thus they can not obtain the depth measurements to those objects. While the key-frame fusion algorithm in (25) requires the complementary information from non-key-frames, hence it cannot work in such situation. Using Kinect camera, Fig. 11 (b) and (c) presents the 3-D map of a room, where large featureless area and pseudo visual features produced by pieces of glasses can be seen. However, the challenging scenes have little impact on the performance of our proposed method, which is insensitive to the visual corner outliers. This can be compared with our previous work [51], which also generates dense maps for the same room. However, it is based on the ultra-wideband (UWB) technology to correct the large visual drift, which requires external UWB anchors. It can be noticed that the improvement in this paper is such that the external sensors are not needed any more to generate dense maps.

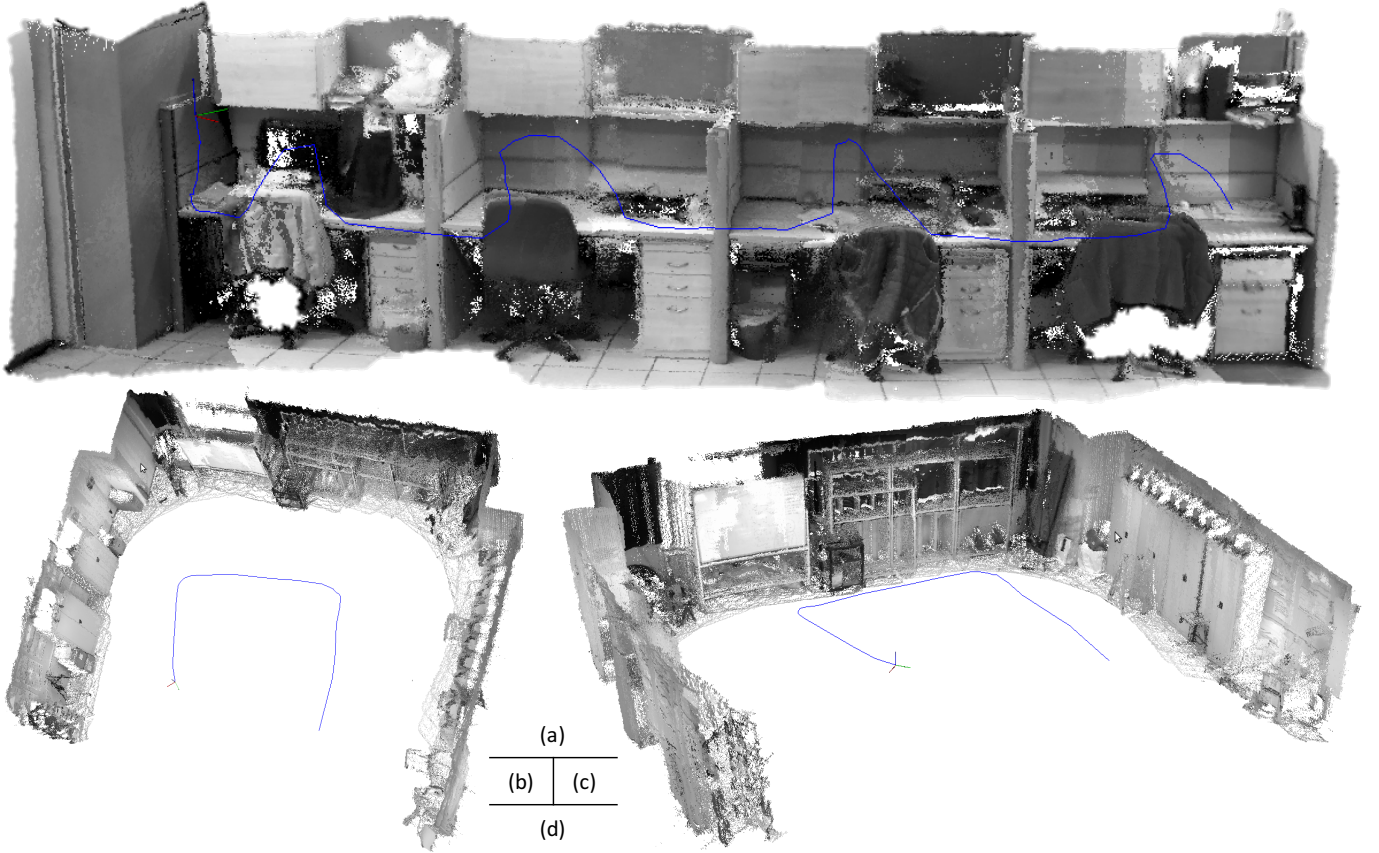


Fig. 11. Figure (a) is the dense reconstruction of office cubicles using the RealSense camera on the ultra low power CPU with Scenario Design Power (SDP) 2W. It is shown without any post-processing. Figure (b) and (c) are the dense room reconstruction map using Kinect from different point of view. The panorama of this room is given in Figure (d) for comparison that large feature-less area and pseudo visual features produced by pieces of glasses can be seen.

TABLE IV

REAL-TIME ACCURACY (m) COMPARISON ON THE STEREO CAMERAS.

Dataset	ours			OKVIS		
	RMSE	MEAN	MAE	RMSE	MEAN	MAE
01_trn	0.091	0.082	0.079	0.128	0.112	0.094
02_htp	0.170	0.159	0.148	0.186	0.161	0.143
03_svo	0.225	0.216	0.217	0.267	0.250	0.261
04_ttr	0.158	0.147	0.155	0.147	0.135	0.150
05_vst	0.099	0.092	0.083	0.124	0.112	0.096
06_bsp	0.091	0.081	0.075	0.110	0.104	0.104
07_llt	0.113	0.102	0.101	0.245	0.236	0.232
overall	0.135	0.126	0.123	0.172	0.159	0.154

TABLE V

AVERAGE RUNNING TIME (ms) COMPARISON USING STEREO CAMERAS.

Dataset	ours			OKVIS	
	track	map	sum.	match	optimize
01_trn	8.6	2.3	10.9	32.0	31.6
02_htp	8.3	2.0	10.3	35.1	30.4
03_svo	8.4	2.7	11.1	38.3	33.8
04_ttr	9.4	1.3	10.7	29.2	29.5
05_vst	8.7	1.6	10.3	36.9	28.4
06_bsp	8.2	2.7	10.9	35.1	35.7
07_llt	8.7	2.7	11.4	30.3	30.1
overall	8.6	2.2	10.8	34.0	31.2

D. Real-Time Performance on Stereo Cameras

Compared with RGB-D cameras, stereo cameras have customized baseline and are insensitive to object materials, but generally produce more depth noises, especially in featureless regions. To show the generality and robustness, performance

on stereo camera is demonstrated in this section. For comparison, the state-of-the-art visual inertial odometry system using stereo cameras, OKVIS [21] is implemented on the same platform mentioned in the Section X-B1. Experimental data is recorded in the same Vicor room using the commercial stereo

camera ZED[®] with the inertial sensor myAHRS+. Based on the software development kit (SDK) of ZED, we are able to obtain stereo images with size 672×376 and 3-D point clouds at 30Hz in ROS. Table IV presents the estimation error where our method shares comparable accuracy compared with OKVIS. The corresponding running time is given in Table V, where our method requires much less running time than OKVIS in all the datasets. Note that OKVIS is based on non-linear optimization and is implemented highly parallel. Hence, the reported data of OKVIS in Table V only indicates the running time of that function, while they cannot be summed up simply. This indicates the proposed method might be able to work for any 3-D sensors that can produce 3-D point clouds. While it is out of our scope to further prove such flexibility.

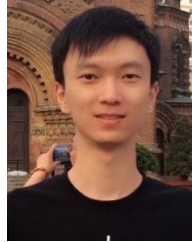
XI. CONCLUSION

In this paper, we proposed a non-iterative framework for real-time localization and dense mapping system using 3-D camera and inertial sensors. It was demonstrated that the traditional 3-D mapping process can be accelerated based on single key-frame training. First, based on the axonometric projection and the proposed adaptive resolution searching algorithm, we are able to decouple 3-D point clouds into several subspaces where camera movements can be estimated respectively. Then by leveraging the property of KCC, we found a non-iterative solution for RGB-D-inertial data association, which is robust to visual feature outliers and significantly decreases the computational burden and makes real-time localization and dense mapping feasible for low power systems. Last, a very fast refinement/fusion method was designed to fill the missing information of key-frames based on moving average. To the best of our knowledge, the proposed framework may be the first non-iterative solution for the front-end of fast dense mapping system and is able to achieve the fastest speed and comparable accuracy compared with the state-of-the-arts.

REFERENCES

- [1] T. Bailey and H. Durrant-Whyte, "Simultaneous Localization and Mapping (SLAM): Part II," *Robotics & Automation Magazine*, vol. 13, no. 3, pp. 108–117, 2006.
- [2] P. Henry, M. Krainin, E. Herbst, X. Ren, and D. Fox, "RGB-D Mapping: Using Kinect-Style Depth Cameras for Dense 3D Modeling of Indoor Environments," *International Journal of Robotics Research*, vol. 31, no. 5, pp. 647–663, Apr. 2012.
- [3] J. Fuentes-Pacheco, J. Ruiz-Ascencio, and J. M. Rendón-Mancha, "Visual simultaneous localization and mapping: a survey," *Artificial Intelligence Review*, vol. 43, no. 1, pp. 55–81, Nov. 2012.
- [4] P. J. Besl and N. D. McKay, "A Method for Registration of 3-D Shapes," *IEEE Transactions on Pattern Analysis and Machine Intelligence*, vol. 14, pp. 1–18, Feb. 1992.
- [5] R. A. Newcombe, A. J. Davison, S. Izadi, P. Kohli, O. Hilliges, J. Shotton, D. Molyneaux, S. Hodges, D. Kim, and A. Fitzgibbon, "KinectFusion: Real-Time Dense Surface Mapping and Tracking," in *2011 IEEE International Symposium on Mixed and Augmented Reality*. IEEE, 2011, pp. 127–136.
- [6] T. Whelan, M. Kaess, M. Fallon, and H. Johansson, "Kintinuous: Spatially extended kinectfusion," *RSS Workshop on RGB-D Advanced Reasoning with Depth Cameras*, 2012.
- [7] T. Whelan, S. Leutenegger, R. Salas Moreno, B. Glocker, and A. Davison, "ElasticFusion: Dense SLAM Without A Pose Graph," in *Robotics: Science and Systems*. Robotics: Science and Systems Foundation, Jul. 2015.
- [8] T. Whelan, R. F. Salas-Moreno, B. Glocker, A. J. Davison, and S. Leutenegger, "ElasticFusion: Real-time dense SLAM and light source estimation," *International Journal of Robotics Research*, Sep. 2016.
- [9] R. A. Newcombe, D. Fox, and S. M. Seitz, "DynamicFusion: Reconstruction and Tracking of Non-Rigid Scenes in Real-Time," in *IEEE Conference on Computer Vision and Pattern Recognition*. IEEE, 2015, pp. 343–352.
- [10] A. J. Davison, I. D. Reid, N. D. Molton, and O. Stasse, "MonoSLAM: Real-Time Single Camera SLAM," *IEEE Transactions on Pattern Analysis and Machine Intelligence*, vol. 29, no. 6, pp. 1052–1067, Apr. 2007.
- [11] G. Klein and D. Murray, "Parallel Tracking and Mapping for Small AR Workspaces," *2007 6th IEEE and ACM International Symposium on Mixed and Augmented Reality*, pp. 225–234, 2007.
- [12] C. Forster, M. Pizzoli, and D. Scaramuzza, "SVO: Fast Semi-Direct Monocular Visual Odometry," in *IEEE International Conference on Robotics and Automation (ICRA)*. IEEE, 2014, pp. 15–22.
- [13] R. Mur-Artal, J. M. M. Montiel, and J. D. Tardos, "ORB-SLAM: A Versatile and Accurate Monocular SLAM System," *IEEE Transactions on Robotics*, vol. 31, no. 5, pp. 1147–1163, 2015.
- [14] C. Kerl, J. Sturm, and D. Cremers, "Dense Visual SLAM for RGB-D Cameras," in *IEEE/RSJ International Conference on Intelligent Robots and Systems (IROS)*. IEEE, 2013, pp. 2100–2106.
- [15] —, "Robust odometry estimation for RGB-D cameras," in *IEEE International Conference on Robotics and Automation (ICRA)*. IEEE, 2013, pp. 3748–3754.
- [16] D. Gutierrez-Gomez, W. Mayol-Cuevas, and J. J. Guerrero, "Dense RGB-D Visual Odometry Using Inverse Depth," *Robotics and Autonomous Systems*, vol. 75, pp. 571–583, 2016.
- [17] J. Engel, T. Schöps, and D. Cremers, "LSD-SLAM: Large-Scale Direct Monocular SLAM," in *European Conference on Computer Vision*. Switzerland: Springer International Publishing, 2014, pp. 834–849.
- [18] R. A. Newcombe, S. J. Lovegrove, and A. J. Davison, "DTAM: Dense Tracking and Mapping in Real-Time," in *IEEE International Conference on Computer Vision*. IEEE, 2011, pp. 2320–2327.
- [19] F. Endres, J. Hess, J. Sturm, D. Cremers, and W. Burgard, "3-D Mapping With an RGB-D Camera," *IEEE Transactions on Robotics*, vol. 30, no. 1, pp. 177–187, 2014.
- [20] A. Concha, G. Loianno, V. Kumar, and J. Civera, "Visual-Inertial Direct SLAM," in *IEEE International Conference on Robotics and Automation (ICRA)*. IEEE, 2016, pp. 1331–1338.
- [21] S. Leutenegger, S. Lynen, M. Bosse, R. Siegwart, and P. Furgale, "Keyframe-Based Visual-Inertial Odometry Using Nonlinear Optimization," *International Journal of Robotics Research*, vol. 34, no. 3, pp. 314–334, Feb. 2015.
- [22] T. Laidlow, M. Bloesch, W. Li, and S. Leutenegger, "Dense RGB-D-Inertial SLAM with Map Deformations," in *IEEE/RSJ International Conference on Intelligent Robots and Systems (IROS)*, 2017, pp. 6741–6748.
- [23] R. Raguram, J.-M. Frahm, and M. Pollefeys, "A Comparative Analysis of RANSAC Techniques Leading to Adaptive Real-Time Random Sample Consensus," in *Computer Vision – ECCV 2008*. Berlin, Heidelberg: Springer, Berlin, Heidelberg, Oct. 2008, pp. 500–513.
- [24] G. Costante, M. Mancini, and P. Valigi, "Exploring Representation Learning With CNNs for Frame-to-Frame Ego-Motion Estimation," *IEEE Robotics and Automation Letters*, vol. 1, no. 1, pp. 18–25, 2016.
- [25] V. Mohanty, S. Agrawal, S. Datta, A. Ghosh, V. D. Sharma, and D. Chakravarty, "DeepVO: A Deep Learning approach for Monocular Visual Odometry," *arXiv.org*, p. arXiv:1611.06069, 2016.
- [26] K. Tateno, F. Tombari, I. Laina, and N. Navab, "CNN-SLAM: Real-time dense monocular SLAM with learned depth prediction," *arXiv.org*, p. arXiv:1704.03489, 2017.
- [27] R. Clark, S. Wang, H. Wen, A. Markham, and N. Trigoni, "VINet: Visual-Inertial Odometry as a Sequence-to-Sequence Learning Problem," *arXiv.org*, p. arXiv:1701.08376, 2017.
- [28] D. DeTone, T. Malisiewicz, and A. Rabinovich, "Toward Geometric Deep SLAM," *arXiv.org*, p. arXiv:1707.07410, Jul. 2017.
- [29] C. Wang, J. Yuan, and L. Xie, "Non-Iterative SLAM," in *2017 18th International Conference on Advanced Robotics (ICAR)*. Hong Kong: IEEE, Jul. 2017, pp. 83–90.
- [30] J. F. Henriques, R. Caseiro, and P. Martins, "High-Speed Tracking with Kernelized Correlation Filters," *IEEE Transactions on Pattern Analysis and Machine Intelligence*, vol. 37, no. 3, pp. 583–596, 2015.
- [31] C. Wang, L. Zhang, L. Xie, and J. Yuan, "Kernel Cross-Correlator," *arXiv.org*, p. arXiv:1709.05936, Sep. 2017.
- [32] T. Whelan, M. Kaess, H. Johansson, M. Fallon, J. J. Leonard, and J. McDonald, "Real-Time Large-Scale Dense RGB-D SLAM with

- Volumetric Fusion,” *International Journal of Robotics Research*, vol. 34, no. 4-5, pp. 598–626, 2015.
- [33] A. Dai, M. Nießner, M. Zollhöfer, and S. Izadi, “BundleFusion: Real-time Globally Consistent 3D Reconstruction using On-the-fly Surface Reintegration,” *ACM Transactions on Graphics*, vol. 36, no. 3, pp. 1–18, 2017.
- [34] F. Fraundorfer and D. Scaramuzza, “Visual Odometry: Part II: Matching, Robustness, Optimization, and Applications,” *Robotics & Automation Magazine*, vol. 19, no. 2, pp. 78–90, May 2012.
- [35] S. Khan and D. Wollherr, “IBUILD: Incremental bag of Binary words for appearance based loop closure detection,” in *IEEE International Conference on Robotics and Automation (ICRA)*. IEEE, 2015, pp. 5441–5447.
- [36] J. Engel, J. Stuckler, and D. Cremers, “Large-Scale Direct SLAM with Stereo Cameras,” in *IEEE/RSJ International Conference on Intelligent Robots and Systems (IROS)*. IEEE, 2015, pp. 1935–1942.
- [37] J. Engel, V. Koltun, and D. Cremers, “Direct Sparse Odometry,” *IEEE Transactions on Pattern Analysis and Machine Intelligence*, Apr. 2017.
- [38] S. Weiss and R. Siegwart, “Real-Time Metric State Estimation for Modular Vision-Inertial Systems,” in *IEEE International Conference on Robotics and Automation (ICRA)*. IEEE, 2011, pp. 4531–4537.
- [39] S. Lynen, M. W. Achtelik, S. Weiss, M. Chli, and R. Y. S. Ingénieur mécanicien, “A Robust and Modular Multi-Sensor Fusion Approach Applied to MAV Navigation,” in *IEEE/RSJ International Conference on Intelligent Robots and Systems (IROS)*, 2013.
- [40] K. Konolige, M. Agrawal, and J. Solà, “Large-Scale Visual Odometry for Rough Terrain,” Springer Berlin Heidelberg, Berlin, Heidelberg, 2010.
- [41] A. I. Mourikis and S. I. Roumeliotis, “A Multi-State Constraint Kalman Filter for Vision-aided Inertial Navigation,” in *IEEE International Conference on Robotics and Automation (ICRA)*. IEEE, 2015, pp. 3565–3572.
- [42] M. Li and A. I. Mourikis, “High-Precision, Consistent EKF-Based Visual-Inertial Odometry,” *International Journal of Robotics Research*, vol. 32, no. 6, pp. 690–711, 2013.
- [43] C. Forster, L. Carlone, F. Dellaert, and D. Scaramuzza, “IMU Preintegration on Manifold for Efficient Visual-Inertial Maximum-a-Posteriori Estimation,” in *Robotics: Science and Systems*. Robotics: Science and Systems Foundation, Jul. 2015.
- [44] L. Ma, J. M. Falquez, S. McGuire, and G. Sibley, “Large scale dense visual inertial slam,” *Field and Service Robotics*, 2016.
- [45] N. Engelhard, F. Endres, and J. Hess, “Real-time 3D visual SLAM with a hand-held RGB-D camera,” *Proc. of the RGB-D Workshop on 3D Perception in Robotics at the European Robotics Forum, Vasteras, Sweden*, vol. 180, 2011.
- [46] Y. Ji, A. Yamashita, and H. Asama, “RGB-D SLAM Using Vanishing Point and Door Plate Information in Corridor Environment,” *Intelligent Service Robotics*, vol. 8, no. 2, pp. 105–114, 2015.
- [47] S. Omari, M. Bloesch, P. Gohl, and R. Siegwart, “Dense Visual-Inertial Navigation System for Mobile Robots,” in *IEEE International Conference on Robotics and Automation (ICRA)*. IEEE, 2015, pp. 2634–2640.
- [48] A. Makadia, A. I. Patterson, and K. Daniilidis, “Fully Automatic Registration of 3D Point Clouds,” in *2006 IEEE Computer Society Conference on Computer Vision and Pattern Recognition - Volume 1 (CVPR’06)*. IEEE, 2006, pp. 1297–1304.
- [49] D. Bolme, J. R. Beveridge, B. A. Draper, and Y. M. Lui, “Visual Object Tracking Using Adaptive Correlation Filters,” in *IEEE Conference on Computer Vision and Pattern Recognition*. IEEE, 2010, pp. 2544–2550.
- [50] J. W. Langelaan, “State Estimation for Autonomous Flight in Cluttered Environments,” *Journal of Guidance, Control, and Dynamics*, vol. 30, no. 5, pp. 1414–1426, 2007.
- [51] C. Wang, H. Zhang, T.-M. Nguyen, and L. Xie, “Ultra-Wideband Aided Fast Localization and Mapping System,” in *IEEE/RSJ International Conference on Intelligent Robots and Systems (IROS)*, Sep. 2017, pp. 1602–1609.
- [52] R. Mur-Artal and J. D. Tardós, “ORB-SLAM2: An Open-Source SLAM System for Monocular, Stereo, and RGB-D Cameras,” *IEEE Transactions on Robotics*, pp. 1–8, 2017.
- [53] D. Galvez-Lopez and J. D. Tardós, “Bags of Binary Words for Fast Place Recognition in Image Sequences,” *IEEE Transactions on Robotics*, vol. 28, no. 5, pp. 1188–1197, Oct. 2012.
- [54] A. Glover, W. Maddern, M. Warren, S. Reid, M. Milford, and G. Wyeth, “OpenFABMAP: an Open Source Toolbox for Appearance-Based Loop Closure Detection,” in *IEEE International Conference on Robotics and Automation (ICRA)*. IEEE, May 2012, pp. 4730–4735.
- [55] R. Kummerle, G. Grisetti, H. Strasdat, K. Konolige, and W. Burgard, “G2O: a General Framework for Graph Optimization,” in *IEEE International Conference on Robotics and Automation (ICRA)*. IEEE, 2011, pp. 3607–3613.



Chen Wang received the B.Eng. degree in electrical engineering from Beijing Institute of Technology (BIT), China, in 2014. He is currently pursuing the Ph.D. degree with the School of Electrical and Electronic Engineering, Nanyang Technological University, Singapore. He received the Best Paper Award from 2017 18th International Conference on Advanced Robotics (ICAR 2017). His research interests include robot perception, machine learning, and artificial intelligence.



Lihua Xie received the B.E. and M.E. degrees in electrical engineering from Nanjing University of Science and Technology in 1983 and 1986, respectively, and the Ph.D. degree in electrical engineering from the University of Newcastle, Australia, in 1992. Since 1992, he has been with the School of Electrical and Electronic Engineering, Nanyang Technological University, Singapore, where he is currently a professor and Director, Delta-NTU Corporate Laboratory for Cyber-Physical Systems. He served as the Head of Division of Control and Instrumentation from July 2011 to June 2014. He held teaching appointments in the Department of Automatic Control, Nanjing University of Science and Technology from 1986 to 1989.

Dr Xie’s research interests include robust control and estimation, networked control systems, multi-agent networks, localization and unmanned systems. He is an Editor-in-Chief for Unmanned Systems and an Associate Editor for IEEE Transactions on Network Control Systems. He has served as an editor of IET Book Series in Control and an Associate Editor of a number of journals including IEEE Transactions on Automatic Control, Automatica, IEEE Transactions on Control Systems Technology, and IEEE Transactions on Circuits and Systems-II. He is an elected member of Board of Governors, IEEE Control System Society (Jan 2016-Dec 2018). Dr. Xie is a Fellow of IEEE and Fellow of IFAC.



Junsong Yuan is currently an Associate Professor at School of Electrical and Electronics Engineering (EEE), Nanyang Technological University (NTU), Singapore. He received Ph.D. from Northwestern University in 2009. He is an Associate Editor of IEEE Trans. on Image Processing (T-IP), IEEE Trans. on Circuits and Systems for Video Technology (T-CSVT) and The Visual Computer journal (TVC). He is Program Co-Chair of ICME18 and Area Chair of CVPR17, ICIP17, ICPR16, ACCV14, etc. He received 2016 Best Paper Award from IEEE Trans. on Multimedia (T-MM), Doctoral Spotlight Award from IEEE Conf. on Computer Vision and Pattern Recognition (CVPR’09), Nanyang Assistant Professorship from NTU, and Outstanding EECS Ph.D. Thesis award from Northwestern University.